Aerotecnica Missili & Spazio (2023) 102:323–335
https://doi.org/10.1007/s42496-023-00169-2

ORIGINAL ARTICLE

Simulation of High-Enthalpy Turbulent Shock Wave/Boundary Layer Interaction Using a RANS Approach

Davide Ninni[1] · **Francesco Bonelli**[1] · **Giuseppe Pascazio**[1]

Received: 16 June 2023 / Revised: 4 August 2023 / Accepted: 8 August 2023 / Published online: 30 August 2023
© The Author(s) 2023

Abstract
In the era of space exploration, the scientific community is strongly focusing on the analysis of hypersonic flows in the presence of shock wave/boundary layer interaction. In these conditions, the flow field presents a complex shock structure due to the interaction of different shock waves with the boundary layer. The strong adverse pressure gradient makes the boundary layer separate, giving rise to a separation bubble. In the reattachment zone, the temperature can reach very high values, inducing thermochemical non-equilibrium effects. This research field is recently achieving more and more relevance in aerospace research, as the analysis of turbulent shock wave/boundary layer interaction so far has been mainly focused on perfect gas flows. In this manuscript, a Reynolds averaged Navier–Stokes (RANS) approach is considered, the shear stress transport (SST) model being coupled with the multitemperature approach proposed by Park to investigate thermochemical non-equilibrium effects in hypersonic turbulent shock wave/boundary layer interaction. The first part of the manuscript is devoted to the validation of the solver, and results for low enthalpy flat plate and compression ramp flows are presented. The numerical results are shown to be in good agreement with numerical solutions and experimental measurements. Afterward, the free stream conditions are modulated to make non-equilibrium relevant and analyze a reacting flow.

Keywords Hypersonic flow · Boundary layer · Shock wave/boundary layer interaction · Turbulence · CUDA

1 Introduction

The scientific community is currently devoting a lot of efforts to the numerical investigation of turbulent boundary layers, especially in the context of hypersonic flight, due to its impact for several breakthrough applications such as military or space exploration [1]. At hypersonic speeds, most of the kinetic energy of the flow is converted to internal energy, leading to excitation of internal modes of energy (translational, rotational, vibrational and electronic). Moreover, the high temperature reached (≈ 10000 K) induces molecular dissociation and ionization, making the prediction of the flow feature very challenging [2]. Most of the times, experiments are very hard to carry out due to the difficulties encountered in the physical reproduction of the flight conditions [3], making numerical simulations a valid alternative for the accurate evaluation of the main flow field characteristics (chemical composition, shear stresses, heat flux).

In this scenario, turbulence introduces more and more difficulties when solving the Navier–Stokes equations for simulating hypersonic re-entry. A direct numerical simulation (DNS) represents the most accurate and high-fidelity approach for the correct evaluation of the flow features, as all the turbulence scales are resolved. However, the huge computational cost and high order schemes required by such simulations often limit a DNS approach to restricted Reynolds numbers and simple configurations such as flat plate or wall-bounded flows. A wide field of numerical studies is available in the literature for both supersonic [4–7] and hypersonic [8–12] regimes, also accounting for high-temperature effects [13–15]. These works focused on the validity of Morkovin's hypothesis [16], which states that

Francesco Bonelli and Giuseppe Pascazio contributed equally to this work.

✉ Davide Ninni
davide.ninni@poliba.it

Francesco Bonelli
francesco.bonelli@poliba.it

Giuseppe Pascazio
giuseppe.pascazio@poliba.it

[1] Dipartimento di Meccanica, Matematica e Management, Politecnico di Bari, Via Re David 200, Bari 70125, Italy

compressibility effects can be taken into account considering the variation of mean fluid density; the velocity transformation obtained by means of the law of the wall proposed by Van Driest [17–19] is coherent with the incompressible version also for moderate wall and boundary layer edge temperature ratios [9]. However, the assumption of an isothermal, cooled surface is essential in the context of hypersonic flight as it is more realistic [20, 21]. Many authors found that Morkovin's hypothesis breaks down in the presence of relevant wall cooling [9, 22].

One of the most relevant phenomena in turbulence is the shock wave/boundary layer interaction (SWBLI), whose analysis is fundamental for a proper design of the aerodynamic shape of space vehicles. It is typical of complex configurations such as ramp, double-wedge or double-cone geometries: the boundary layer interacts with the shock wave inducing the laminar–turbulent transition [23–25]. The SWBLI can be forced by employing a shock generator which makes the wave interact with the flow over a flat plate, provoking the turbulent transition [25–28]. However, natural SWBLI interaction is induced by the wall deflection, typical of compression ramp geometries. Many researchers have analyzed the turbulent shock wave/boundary layer interaction in high-speed compression ramp flows [29–32]. Given the high computational cost required by compression ramp simulations, these works are mainly based on the use of turbulent models, with some exception [33, 34]. In the framework of hypersonic flows, non-equilibrium conditions have been investigated for different configurations [35–37], also by means of modal analysis [38, 39].

This work aims at assessing the capabilities of an in-house GPU based solver to investigate hypersonic flows in the presence of thermochemical non-equilibrium and turbulent shock wave/boundary layer interaction. Turbulence is modeled by a RANS approach in conjunction with the well-known two-equation shear-stress-transport ($k-\omega$ SST) turbulence model [40]. Such an approach allows to switch from the classical $k-\varepsilon$ model in the far field region to the $k-\omega$ model near the wall, combining the characteristics of both models. Non-equilibrium is modeled through the multi-temperature model proposed by Park [41], hence considering the high temperature effects making the calorically perfect gas assumption no longer valid. Therefore, the mixture is composed of five species (N_2, O_2, NO, N, O) interacting with each other. A continuity equation is solved for each species in the mixture and, also, a transport equation for the vibrational energy of molecules is needed. For this reason, an MPI-CUDA environment is developed to exploit multi-GPU executions and drastically reduce the computational cost [42].

The paper is organized as follows: firstly, the methodology is illustrated, giving details about the governing equations, models and numerical scheme. Afterward, the numerical results are discussed for perfect gas flows, to isolate the turbulence phenomena and assess the effectiveness and accuracy of the model. More in detail, a flat plate and compression ramp flows are investigated. In the final part, thermochemical non-equilibrium conditions are analyzed for the flow over a compression ramp. These must be considered as preliminary results, useful as benchmark for future works.

2 Methodology

2.1 Governing Equations

The system of Navier–Stokes equations is coupled with the SST turbulence model [40] and with the multitemperature model proposed by Park [41] to deal with thermochemical non-equilibrium. The SST model combines two classical turbulence models, namely, the $k-\omega$ and the $k-\varepsilon$ model, and it is widely used in the literature [37, 43, 44]. In the following, the equations describe the mean flow field obtained by performing the Favre (density-weighted) averaging: for a given variable ϕ, $\overline{\phi}=\phi-\phi'$ indicates the standard time average, with ϕ' the corresponding fluctuation, whereas $\widetilde{\phi}=\phi-\phi''=\overline{\rho\phi}/\overline{\rho}$ denotes the density-weighted Favre averaging, with ϕ'' the Favre fluctuation. However, to simplify the notation, overbars and tildes are omitted. To model turbulence high-temperature effects, the model proposed by Jiang et al. [37] has been implemented with few modifications.

Dealing with a multispecies mixture, a continuity equation is solved for each species:

$$\frac{\partial \rho_s}{\partial t}+\nabla\cdot\left(\rho_s\mathbf{u}+\boldsymbol{j}_s\right)=\dot{\omega}_s, \tag{1}$$

where subscript s indicates the *s-th* species in the mixture and $\boldsymbol{j}_s$ is the diffusive flux which accounts for mass diffusion phenomena. This is modeled by means of Fick's law:

$$\boldsymbol{j}_s=-\rho\mathcal{D}_s\nabla Y_s+\rho_s\sum_s\mathcal{D}_s\nabla Y_s-\frac{\mu_T}{Sc_T}\nabla Y_s, \tag{2}$$

with μ_T the turbulent viscosity, $\mathcal{D}_s$ the equivalent diffusion coefficient [48] and $Sc_T=0.9$ the turbulent Schmidt number (equal for all the species). The turbulent viscosity is defined as follows [45]:

$$\mu_T=\frac{\rho a^* k_T}{\max\left(a^*\omega, SF_2\right)}, \tag{3}$$

with $a^*=0.31$. k_T is the turbulent kinetic energy, ω the specific dissipation rate and S the mean strain rate tensor, given by the symmetric part of the gradient of the velocity vector $\mathbf{u}$

$$S_{i,j}=\frac{1}{2}\left(\frac{\partial u_i}{\partial x_j}+\frac{\partial u_j}{\partial x_i}\right). \tag{4}$$

In the definition of μ_T, the term F_2 is

$$F_2 = \tanh\left(argF_2^2\right) \qquad \text{with}$$
$$argF_2 = \max\left(\frac{500\mu_L}{\rho d^2\omega}, \frac{2\sqrt{k_T}}{\beta^*\omega d}\right) \tag{5}$$

with d being the distance from the wall and $\beta^* = 0.09$. The source term in Eq. (1), $\dot{\omega}_s$, is expressed using the law of mass action. More details are given in [42, 46]. Momentum balance reads:

$$\frac{\partial \rho \mathbf{u}}{\partial t} + \nabla \cdot \left[\rho \mathbf{u} \cdot \mathbf{u} + p\bar{\bar{\mathrm{I}}} - (\bar{\bar{\sigma}}_L + \bar{\bar{\sigma}}_T)\right] = 0, \tag{6}$$

where $\sigma_{i,j}^L$ and $\sigma_{i,j}^T$ denote the viscous and turbulent stress tensors, given by the following expressions:

$$\begin{cases} \sigma_{i,j,L} = \mu_L\left[\left(\frac{\partial u_i}{\partial x_j} + \frac{\partial u_j}{\partial x_i}\right) - \frac{2}{3}\frac{\partial u_k}{\partial x_k}\delta_{i,j}\right] \\ \sigma_{i,j,T} = \mu_T\left[\left(\frac{\partial u_i}{\partial x_j} + \frac{\partial u_j}{\partial x_i}\right) - \frac{2}{3}\frac{\partial u_k}{\partial x_k}\delta_{i,j}\right] - \frac{2}{3}\rho k_T \delta_{i,j} \end{cases}, \tag{7}$$

leading to the definition of the "total" stress tensor, given by:

$$\begin{aligned} \sigma_{i,j} &= \sigma_{i,j,L} + \sigma_{i,j,T} \\ &= \left(\mu_L + \mu_T\right)\left[\left(\frac{\partial u_i}{\partial x_j} + \frac{\partial u_j}{\partial x_i}\right) - \frac{2}{3}\frac{\partial u_k}{\partial x_k}\delta_{i,j}\right] - \frac{2}{3}\rho k_T \delta_{i,j}, \end{aligned} \tag{8}$$

where $\delta_{i,j}$ is the Kronecker delta and k_T the turbulent kinetic energy. The molecular viscosity μ_L is computed by means of Wilke's mixing rule [47], which combines single species properties evaluated using Gupta's fitting [48]. The introduction of the turbulent viscosity arises from the Boussinesq assumption: the stresses deriving from the turbulence behave as the molecular ones, but are linked to the flow property (μ_T) instead of depending on a fluid property (μ_L). The term $-\frac{2}{3}\rho k_T \delta_{i,j}$ represents a closure term for a consistent definition of the trace of the Reynolds stress tensor [40].

The total energy conservation accounts for the turbulent stress tensor, the turbulent heat flux and the turbulent transport:

$$\begin{aligned} &\frac{\partial \rho E}{\partial t} + \nabla \cdot \Big[(\rho E + p) \cdot \mathbf{u} - \mathbf{u} \cdot (\bar{\bar{\sigma}}_L + \bar{\bar{\sigma}}_T) \\ &+ (\mathbf{q}_L + \mathbf{q}_T) - \left(\mu_L + \sigma_k \mu_T\right)\nabla k_T\Big] = 0, \end{aligned} \tag{9}$$

with $\sigma_k = 0.85$ [49] and E being the total energy content, accounting also for the turbulent kinetic contribution. Before going into the details of the turbulence modeling, one should recall that, dealing with non-equilibrium flows, the total heat flux is given by three contributions:

$$\mathbf{q}_L = -\lambda_L^{tr}\nabla T^{tr} - \sum_{m=1}^{N_m} \lambda_{m,L}^{vib}\nabla T_m^{vib} + \sum_{s=1}^{N_s} \rho h_s \mathcal{D}_s \nabla Y_s, \tag{10}$$

where N_m and N_s are the number of molecules and species in the mixture, whereas h_s is the total specific enthalpy of species s. Molecular (laminar) thermal conductivity of the mixture (λ_L) is calculated through classical mixing rules [50], whereas Eucken formulation [51] is employed for the evaluation of the vibrational conductivity of the molecule m ($\lambda_{m,L}^{vib}$). Concerning the turbulent heat flux, $\mathbf{q}_T$, a definition similar to the one of the turbulent stress tensor is used : it still depends on the temperature gradient of the mean field, but a "turbulent conductivity" is introduced as a function of the turbulent viscosity. First of all, recall that the thermal conductivity is $\lambda = \frac{\mu c_p}{Pr}$, c_p being the constant pressure specific heat and Pr the Prandtl number (in this definition, the energy modes are neglected for simplicity). In this way, one can define the "turbulent conductivity" as:

$$\lambda_T = \frac{\mu_T c_p}{Pr_T} \longrightarrow \begin{cases} \lambda_T^{tr} = \frac{\mu_T c_p^{tr}}{Pr_T} \\ \lambda_{m,T}^{vib} = \frac{\mu_T c_m^{vib}}{Pr_T} \end{cases}, \tag{11}$$

assuming $Pr_T = 0.9$. The vibrational conductivity is written for each molecule as a convention. Furthermore, note that c_m^{vib} does not refer to constant pressure or constant volume specific heat, since $e^{vib} = h^{vib}$. Moreover, to account for turbulent mass diffusion, one can introduce the "turbulent diffusivity" as in the species continuity equations. In this way, the total turbulent heat flux is given by:

$$\mathbf{q}_T = -\lambda_T^{tr}\nabla T^{tr} - \sum_{m=1}^{N_m} \lambda_{m,T}^{vib}\nabla T_m^{vib} + \sum_{s=1}^{N_s} \frac{\mu_T}{Sc_T} h_s \nabla Y_s. \tag{12}$$

Since a multitemperature model is employed to deal with thermochemical non-equilibrium, a transport equation is solved for each vibrational energy:

$$\frac{\partial \rho_m e_m^{vib}}{\partial t} + \nabla \cdot \left[(\rho_m e_m^{vib}) \cdot \mathbf{u} + \mathbf{q}_{m,L}^{vib} + \mathbf{q}_{m,T}^{vib}\right] = \dot{\omega}_m^{vib}, \tag{13}$$

where the subscript m refers to the m-th molecule in the mixture. In this equation, the heat fluxes are expressed as:

$$\begin{cases} \mathbf{q}_{m,L}^{vib} = -\lambda_{m,L}^{vib}\nabla T_m^{vib} + \rho \mathcal{D}_m e_m^{vib}\nabla Y_m \\ \mathbf{q}_{m,T}^{vib} = -\lambda_{m,T}^{vib}\nabla T_m^{vib} + \frac{\mu_T}{Sc_T} e_m^{vib}\nabla Y_m \end{cases}. \tag{14}$$

Details about the source term $\dot{\omega}_m^{vib}$ are given in [42, 46]. Finally, two additional equations are integrated for modeling the turbulence. These read:

$$\frac{\partial \rho k_T}{\partial t} + \nabla \cdot \left[\rho k_T \mathbf{u} - \left(\mu_L + \sigma_k \mu_T\right)\nabla k_T\right] = P_k - D_k, \tag{15}$$

$$\frac{\partial \rho\omega}{\partial t} + \nabla \cdot \left[\rho\omega\mathbf{u} - \left(\mu_L + \sigma_\omega \mu_T\right)\nabla\omega\right] = P_\omega - D_\omega + C_\omega \tag{16}$$

and represent the evolution of the turbulent kinetic energy (k_T) and specific dissipation rate (ω). Formally, these equations are very similar to those previously described, but they present source terms which are responsible for promoting the turbulence: term P identifies production terms, whereas term D identifies dissipation terms. More in detail,

$$P_k = \min\left(P'_k, 10\beta^* \rho k_T \omega\right), \tag{17}$$

$$D_k = \beta^* \rho k_T \omega, \tag{18}$$

with $P'_k = \sigma_{i,j,T} \frac{\partial u_i}{\partial x_j}$ [49]. The limiter on P_k avoids the buildup of turbulence in the stagnation regions [45]. Sometimes, $P'_k = \mu_T S^2$, which is correct for incompressiblw flows, but is still a good approximation also for compressible flows [49]. Concerning Eq. (16), source terms are expressed as

$$P_\omega = \frac{\alpha P'_k}{\nu_T}, \tag{19}$$

$$D_\omega = \beta \rho \omega^2, \tag{20}$$

where $\nu_T = \mu_T/\rho$ is the turbulent kinematic viscosity. α and β appearing in the production and dissipation terms are functions blended by F_1, namely the blending function (varying from 0 to 1) [45]:

$$\begin{cases} \alpha = \alpha_1 F_1 + \alpha_2(1 - F_1), \\ \beta = \beta_1 F_1 + \beta_2(1 - F_1), \end{cases} \text{ with}$$
$$\begin{cases} F_1 = \tanh\left(argF_1^4\right) \\ argF_1 = \min\left[\max\left(\frac{500\mu_L}{\rho d^2 \omega}, \frac{\sqrt{k_T}}{\beta^* \omega d}\right), \frac{4\sigma_{\omega,2}\rho k_T}{CD_{k\omega} d^2}\right], \\ CD_{k\omega} = \max\left(2\rho\sigma_{\omega,2}\frac{1}{\omega}\frac{\partial k_T}{\partial x_j}\frac{\partial \omega}{\partial x_j}, 10^{-10}\right) \end{cases} \tag{21}$$

with d the distance from the wall and the constants $\alpha_1 = 5/9$, $\alpha_2 = 0.44$, $\beta_1 = 0.075$, $\beta_2 = 0.0828$ and $\sigma_{\omega,2} = 0.856$ [37, 49]. Moreover, in Eq. (16), an additional source term appears, namely the cross diffusion C_ω. This term is responsible for making the model adapt itself to $k - \varepsilon$ model in the far field or to $k - \omega$ model in near-wall regions. This term reads:

$$C_\omega = 2(1 - F_1)\rho\sigma_{\omega,2}\frac{1}{\omega}\frac{\partial k_T}{\partial x_j}\frac{\partial \omega}{\partial x_j}. \tag{22}$$

2.2 Boundary Conditions

Supersonic outflow and inflow boundary conditions are applied on the conservative variables of the Navier–Stokes equations. Concerning turbulence variables, their values must be guessed. A typical way is to compute the turbulent kinetic energy as a function of the turbulent intensity [40]

$$I = \frac{V''}{V} = \frac{\sqrt{\frac{1}{3}\left(u''^2 + v''^2 + w''^2\right)}}{V} = \frac{\sqrt{\frac{2}{3}k_T}}{V}, \tag{23}$$

where the double quotes indicate the fluctuations of the velocity. Hence, the free stream inflow condition for k_T is:

$$k_{T,\infty} = \frac{3}{2}(VI)^2, \tag{24}$$

V being the velocity magnitude and I the turbulent intensity. The latter can assume different values, depending on the case [40, 49]: as a first attempt, $I = 1\%$ has been used in this work. Based on the relation between k_T and ω, the free stream value of the specific dissipation rate is:

$$\omega_\infty = \frac{\rho_\infty k_{T,\infty}}{\mu_{T,\infty}}. \tag{25}$$

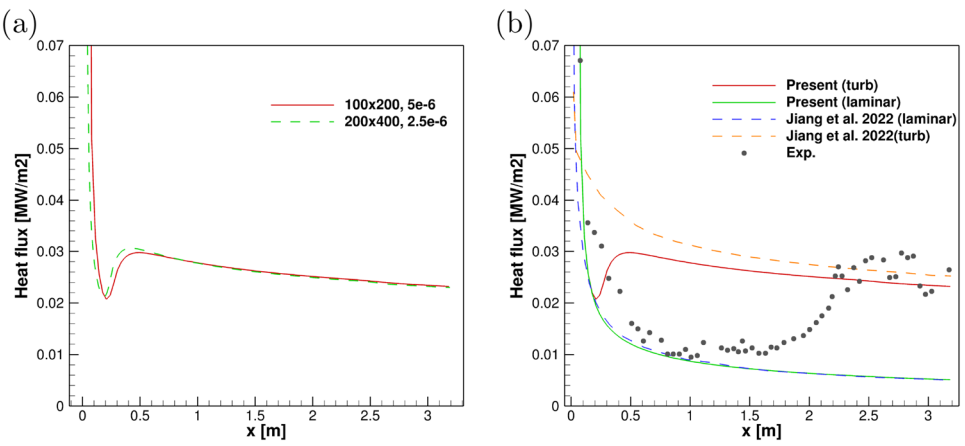

Fig. 1 Heat flux profiles along the wall of the flat plate obtained on the two grids (**a**) and comparison of the results with reference profiles (**b**)

Concerning the boundary conditions, the turbulent kinetic energy k_T must be null at wall

$$k_{T|w} = 0, \tag{26}$$

which implies that $\mu_T = 0$ at wall. The wall boundary condition for ω is [52]:

$$\omega_{|w} = 10\frac{6\nu_L}{\beta_1 d^2}, \tag{27}$$

ν_L being the kinematic viscosity, d the distance of the first point from the wall, and $\beta_1 = 0.075$ [40].

2.3 Numerical Scheme

The governing equations are integrated using a finite-volume scheme implemented in a body-fitted solver. Advection terms are discretized by means of the well-known Steger–Warming flux vector splitting [53], with the right and left state reconstructed through a second-order MUSCL reconstruction [54, 55]. Viscous fluxes are evaluated by means of a second-order centered scheme. Lastly, the time integration is performed in two steps: in the first step, an explicit third-order Runge–Kutta scheme is employed for advancing the homogeneous equations [56]; in the second step, source terms are computed thanks to an implicit iterative Gauss–Seidel scheme [57]. Such an approach (splitting approach) is suitable for reacting flows and it was shown to provide results comparable to fully coupled implicit schemes [46]. The main idea is to employ the most suitable algorithm for treating the different time scales of fluid dynamics and thermochemistry. Solving the coupled equations would drastically reduce the time step size due to the stiffness of the thermochemistry source terms. Instead, the use of a splitting approach allows one to employ an explicit time integration for the fluid dynamics, which involves fewer floating point operations and results in an efficient strategy for GPU implementation. On the other hand, the implicit evaluation of the thermochemistry source terms makes the convergence faster and, involving point operations, maintains the effectiveness of GPU implementation.

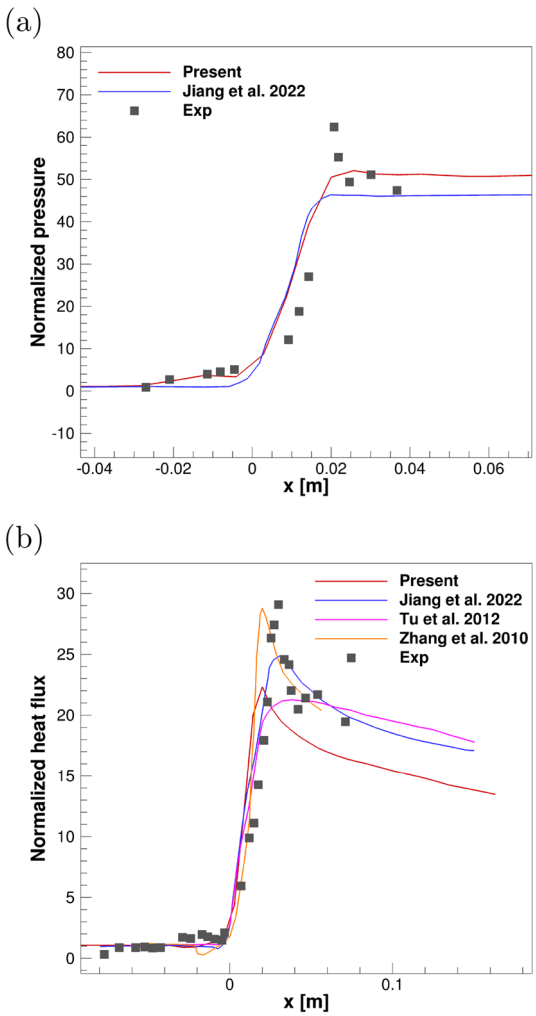

Fig. 3 Normalized pressure (**a**) and heat flux (**b**) along the wall for the low-enthalpy test case

2.3.1 Implicit Formulation for the Source Terms

The solution vector $\tilde{\mathbf{U}} = \left[\rho k_T, \rho\omega\right]^T$ is taken as an example. The tilde indicates that this vector is advanced in time starting from the solution obtained by the first step, namely, from the homogeneous equations, to be updated with the source terms. Hence, one needs to solve the system of equations given by

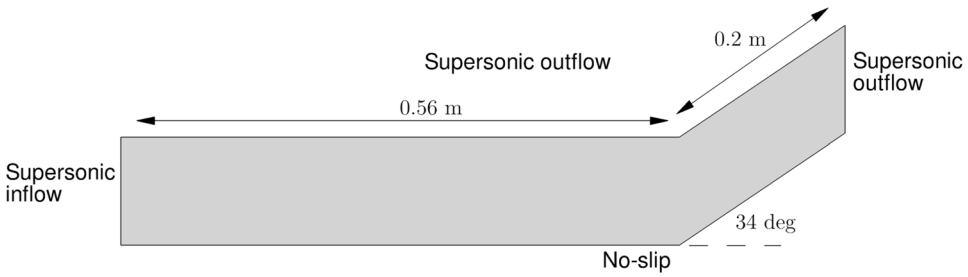

Fig. 2 Computational domain with dimensions and boundary conditions

$$\frac{d\tilde{\mathbf{U}}}{dt} = \mathbf{P} - \overline{\overline{\mathrm{D}}}\tilde{\mathbf{U}}, \tag{28}$$

with $\mathbf{P}$ and $\overline{\overline{\mathrm{D}}}$ a vector and a diagonal matrix whose components are nonnegative and represent the production and dissipation terms for a certain quantity. For turbulence equations, these read:

$$\mathbf{P} = \begin{bmatrix} P_k \\ P_\omega + C_\omega \end{bmatrix} = \begin{bmatrix} \min\left(P'_k, 10\beta^*\rho k_T \omega\right) \\ \alpha \frac{P'_k}{\nu_T} + 2(1-F_1)\rho\sigma_{\omega,2}\frac{1}{\omega}\frac{\partial k_T}{\partial x_j}\frac{\partial \omega}{\partial x_j} \end{bmatrix}, \tag{29}$$

$$\overline{\overline{\mathrm{D}}}\tilde{\mathbf{U}} = \begin{bmatrix} D_k \\ D_\omega \end{bmatrix} = \begin{bmatrix} \beta^*\rho k_T \omega \\ \beta\rho\omega^2 \end{bmatrix} \Longrightarrow \overline{\overline{\mathrm{D}}} = \begin{bmatrix} \beta^*\omega & 0 \\ 0 & \beta\omega \end{bmatrix}. \tag{30}$$

Note that the cross-diffusion term behaves as a production term and has been incorporated into $\mathbf{P}$. For an implicit formulation, the solution vector in the right-hand side of Eq. (28) must be evaluated at the 'new time'. So, indicating with k the *k-th* inner iteration and with n the *n-th* time step, one has:

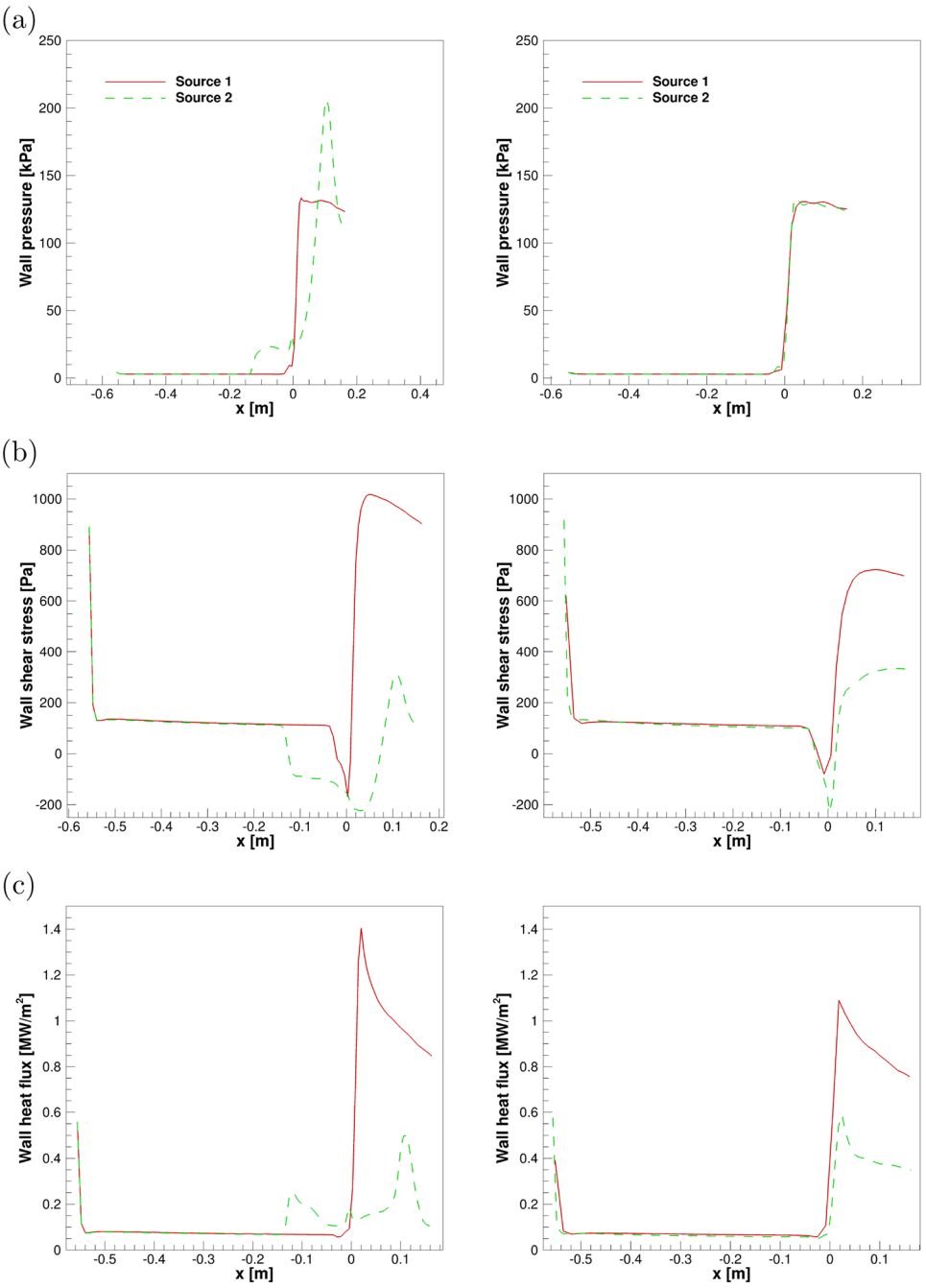

Fig. 4 Comparison of pressure (**a**), shear stress (**b**) and heat flux (**c**) profiles for different expressions of the turbulent kinetic energy production term: medium mesh (left) and coarse mesh (right)

$$\frac{\mathbf{U}^{k+1,n}-\mathbf{U}^{n-1}}{\Delta t}=\mathbf{P}^{k,n}-\overline{\overline{\mathrm{D}}}^{k,n}\,\mathbf{U}^{k+1,n}$$

$$\Longrightarrow \boxed{\mathbf{U}^{k+1,n}=\frac{\mathbf{U}^{n-1}+\Delta t\,\mathbf{P}^{k,n}}{1+\Delta t\,\overline{\overline{\mathrm{D}}}^{k,n}}}. \tag{31}$$

The same approach is applied to evaluate thermochemical source terms. In this work, eight inner iterations are considered for turbulence and four iterations for thermochemistry. This set of inner iterations turned out to provide an effective convergence. Moreover, since no threshold value is imposed for the residuals, GPU threads are ensured to be synchronized during the calculation.

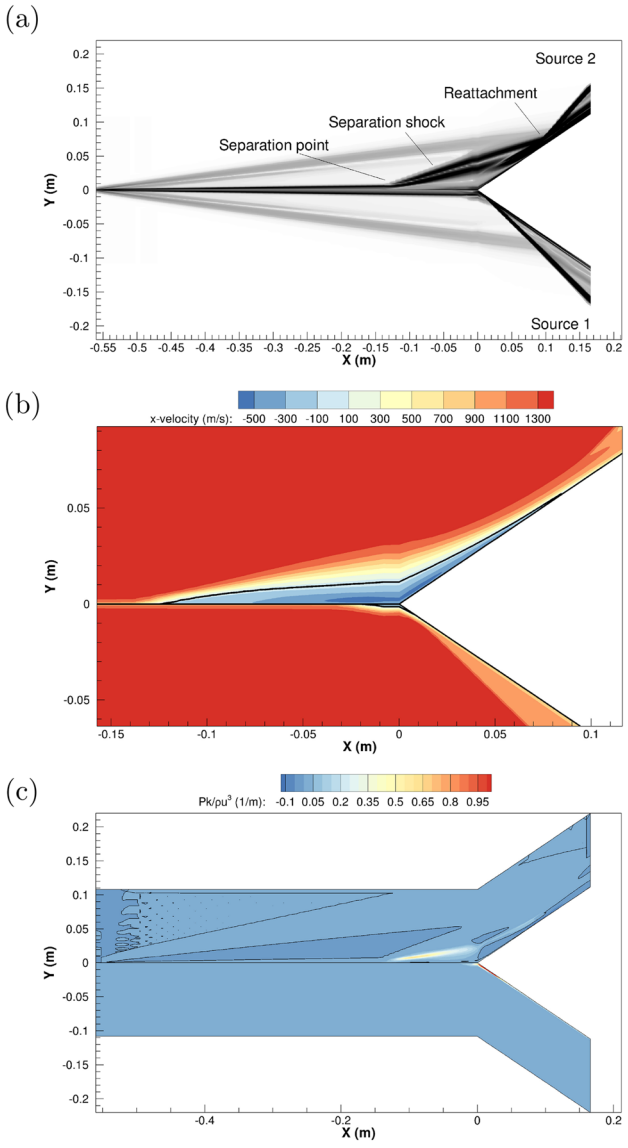

Fig. 5 Schlieren images (**a**), x-velocity contour in the compression corner (**b**) and contour of the normalized source term P_k (**c**) for the low-enthalpy case. Black lines in (**b**) and (**c**) identify the null values

3 Results

3.1 Hypersonic Flow over a Flat Plate (Perfect Gas)

Perfect gas assumption helps in isolating turbulence, neglecting high-temperature effects. Hence, a Mach 7 flow over a flat plate is taken as an example [37, 58, 59]. The sample is 3.2 m long, and two grids were tested to analyze the convergence of the solution. The first computational domain is composed of 100×200 nodes, with a wall resolution of 5×10^{-6} m; the second one is composed of 200×400 nodes, with a wall resolution of 2.5×10^{-6} m. They provide the same results as shown in Fig. 1(a), though a little deviation appears in the transition region. However, this model is not able to capture the laminar-to-turbulent transition, making more relevant the downstream region. The comparison of the wall heat flux with the numerical reference [37] and experimental findings [59] for both laminar and turbulent regimes is shown in Fig. 1(b). The agreement is very satisfactory, even if some discrepancies can be observed. These are attributed to some difference in the turbulence model employed in [37].

3.2 Hypersonic Flow over a Compression Ramp

In this section, the results for the flow over a compression ramp is discussed. The first test aims at the validation of the code. For this purpose, the experiment conducted by Coleman and Stollery [23] is simulated. In such a case, the low free stream enthalpy makes the perfect gas assumption suitable. Once the validation is assessed, the free stream enthalpy is increased to investigate the high-temperature effects. The geometry considered is the same for both cases: a sketch reporting the dimensions of the domain and boundary conditions is illustrated in Fig. 2. The wall is isothermal at $T_w = 295\ K$.

In accordance with references [37, 43, 44], the solver employed a mesh with 100×200 control volumes, distributed so that the height of the first cell at wall is $5 \times 10^{-7}\ m$.

3.2.1 Low-Enthalpy Flow (Perfect Gas)

The test gas is pure nitrogen with free stream density of $\rho_\infty = 0.133894\ kg/m^3$ and temperature $T_\infty = 64.5\ K$. The free stream Mach number is $M_\infty = 9.22$, whereas the free stream Reynolds number (per unit length) is $Re_\infty = 4.7 \times 10^7\ 1/m$. The aforementioned wall resolution results in a value of y^+ of 0.08 near the compression corner. The results are illustrated in Fig. 3, where the profiles of the

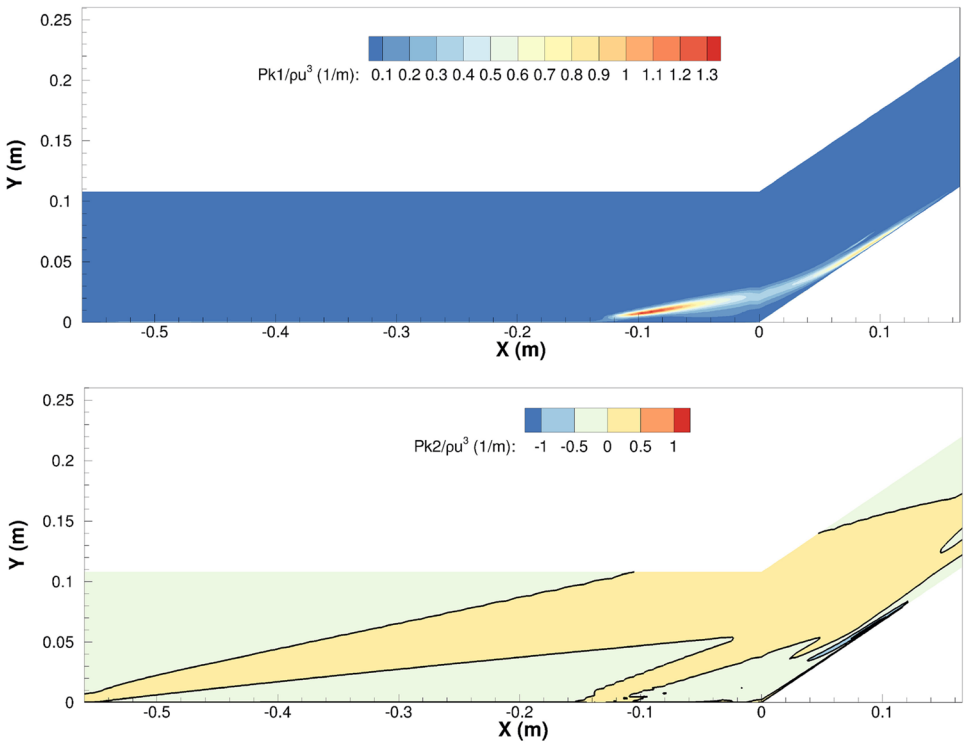

Fig. 6 Contour maps of the two contributions of the turbulent kinetic energy production term for the low-enthalpy case

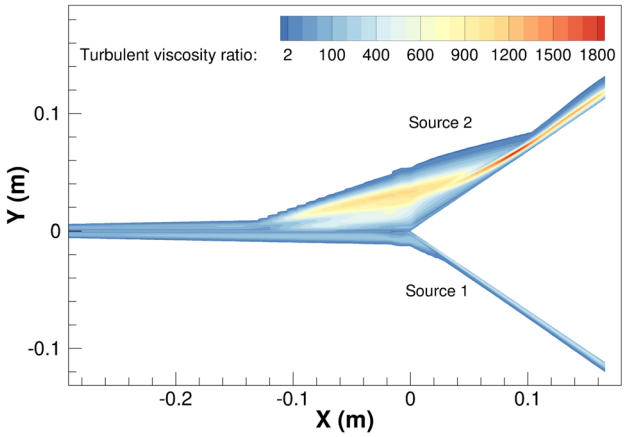

Fig. 7 Contour maps of the turbulent viscosity ratio for the low-enthalpy case

normalized pressure (p_w/p_∞) and heat flux (q_w/q_∞, with $q_\infty = 6.29$ W/cm^2 [58]), are reported and compared with numerical references from the literature [37, 43, 44] and experimental findings.

The results reported by the present simulations are in good agreement with references, with slight underestimation of pressure and heat flux downstream of the corner. Specifically, the pressure profiles are very smooth and present an overall constant value downstream of the shock; contrarily, observing the experimental measurements a peak would be expected. The most critical aspect is the absence of the heat flux jump near the corner ($x \approx -0.3\,m$): the trend found by Zhang [43] is even opposite to the experiments, with the heat flux decreasing toward the wall deflection. Besides these comments, the results are in a good agreement with the expectations.

It is noteworthy that these results were obtained imposing $P'_k = \mu_T S^2$ in Eq. (17), which provides good agreement with the experiments. In fact, within the context of the closure problem in the RANS approach, one of the issues in highly compressible flows is represented by the modeling of the production term of the turbulent kinetic energy equation [60] that is particularly critical in hypersonic flows with shock waves [61]. In Fig. 4, wall quantity profiles are shown for the aforementioned grid and a coarser one (nodes halved in both directions) with $P'_k = \mu_T S^2$ (source 1) and $P'_k = \sigma_{i,j,T}\frac{\partial u_i}{\partial x_j}$ (source 2). Important differences are observed. It is fundamental to highlight that such differences do not appear for the flat plate test case: as a matter of fact, deviations between the two approaches take

Table 1 Free stream conditions for the high-enthalpy test case

M_∞	$h_{0,\infty}$ [MJ/kg K]	Re_∞ [1/m]	T_∞ [K]	p_∞ [Pa]	Y_{N_2}	Y_{O_2}
10	7.4	6.6×10^6	348.6	3596	0.767	0.233

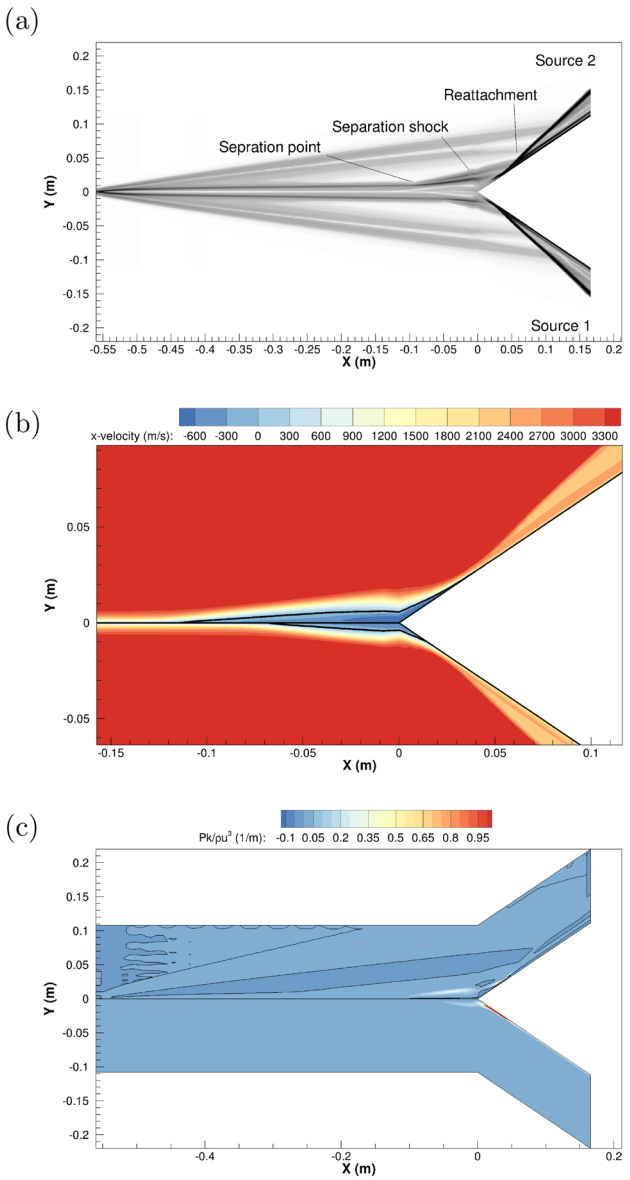

Fig. 8 Schlieren images (**a**), x-velocity in the compression corner (**b**) and contour of the normalized source term P_k (**c**) for the high-enthalpy case. Black lines in (**b**) and (**c**) identify the null values

place from the separation bubble on, whereas they provide the same results in the upstream field (flat plate zone). Furthermore, the authors have experienced similar behavior on finer meshes, but not on coarser ones where the separation point remains unchanged, as reported in the right-hand side of Fig. 4. This behavior, probably linked to numerical modeling issues, needs further investigations which go beyond the scope of the preliminary assessment of this work.

To better understand the wall quantity profiles, Schlieren images were extrapolated from the flow field. They are shown in Fig. 5(a) together with the zoom of the x-velocity contour in the compression corner (Fig. 5(b)) and the contour of the source term P_k, normalized by $\rho_\infty u_\infty^3$ (Fig. 5(c)) (medium mesh). The black lines in figures (b) and (c) identify the null values. A separation shock is formed near the compression corner due to the interaction of the ramp oblique shock with the boundary layer on the flat plate. Hence, a separation region forms downstream of the so-called separation point, where the flow is subsonic. While moving along the deflected wall, the flow reattaches and is again supersonic. The prediction of separation point location is fundamental in view of a full understanding of the involved phenomena.

The source 2 induces a stronger compressibility of the flow due to a stronger separation shock: this is evident also from the pressure peak in Fig. 4(a). Moreover, the separation extent is much larger with respect to the source 1 case: the zoom of the x-velocity puts in evidence how the boundary layer separation is markedly larger and starts more upstream in case of the source 2, pushing the reattachment toward the trailing edge of the ramp. Finally, a completely different behavior is observed for P_k in the source 2 case, which presents large zones with negative values. Also, turbulent kinetic energy production is higher in the case of source 2.

It is fundamental to underline that the production term should be non-negative. *De facto*, $P'_k = \mu_T S^2$ is non-negative, but in the case of source 2 $P'_k = \sigma_{i,j,T}\frac{\partial u_i}{\partial x_j}$. Performing the algebra yields

$$P'_k = \underbrace{\left\{\mu_T\left[\left(\frac{\partial u_i}{\partial x_j}+\frac{\partial u_j}{\partial x_i}\right)-\frac{2}{3}\frac{\partial u_k}{\partial x_k}\delta_{i,j}\right]\right\} : \frac{\partial u_i}{\partial x_j}}_{P_{k1}\geq 0} \underbrace{-\frac{2}{3}\rho k_T \delta_{i,j} : \frac{\partial u_i}{\partial x_j}}_{P_{k2}\lesseqgtr 0}, \tag{32}$$

where the second term is responsible for the change of sign in the global production term. The comparison of these two contributions is reported in Fig. 6. The larger separation encountered in the case of the source 2 induces a larger turbulent viscosity ratio (μ_T/μ_L), as depicted in Fig. 7.

3.2.2 High-Enthalpy Flow (Non-equilibrium)

The numerical simulation of the high-enthalpy flow exploits the same computational domain of the low-enthalpy case. However, to induce relevant non-equilibrium, the free stream conditions are changed as reported in table 1. Adiabatic and no-slip boundary conditions are imposed at wall. It is worth highlighting that the adiabatic condition makes the temperature reach a very high value at the wall: specifically, for this test case it is about 6000 K. Such high values are never

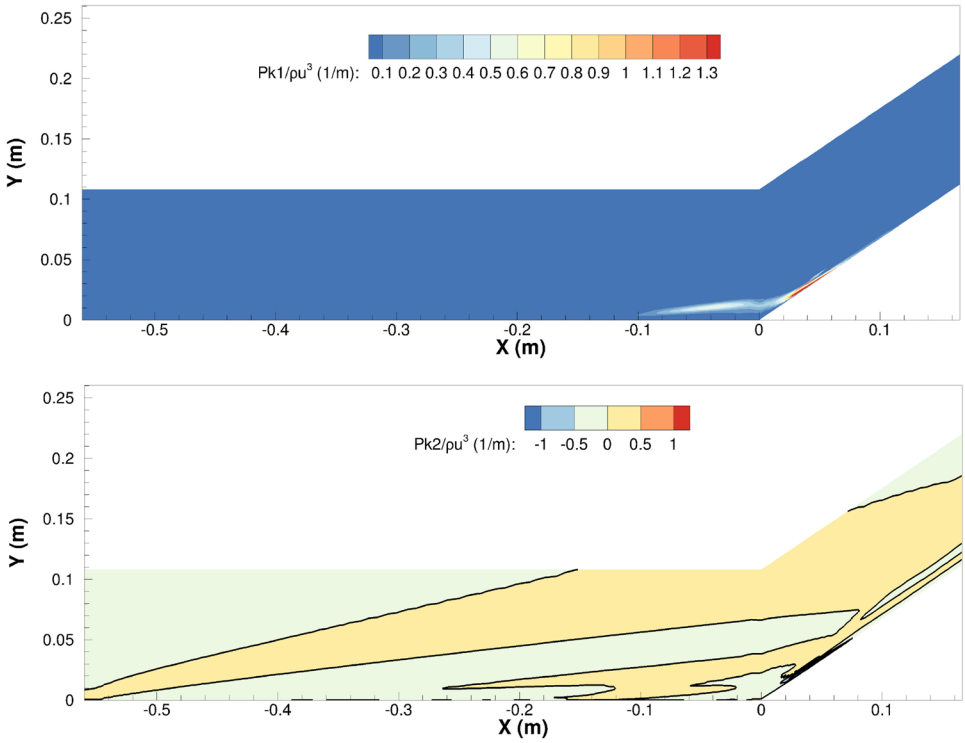

Fig. 9 Contour maps of the two contributions of the turbulent kinetic energy production term for the high-enthalpy case

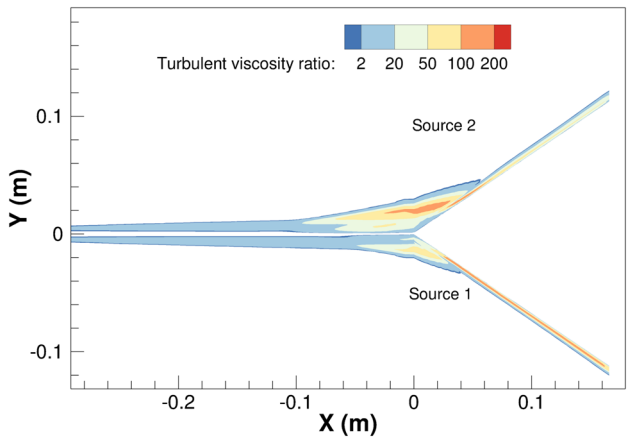

Fig. 10 Contour maps of the turbulent viscosity ratio for the high-enthalpy case

reached in practical problems, as the wall cooling enhances the heat mitigation. However, it is an interesting point to analyze thermochemical non-equilibrium effects in turbulent regime.

Schlieren images, x-velocity and normalized P_k contours are shown in Fig. 8. The separation bubble is bigger if predicted by the source 2 (see Fig. 8(b)). However, the difference is less relevant with respect to the low enthalpy case: indeed, the contour maps of the turbulent kinetic energy production term are quite similar in the two cases (see Fig. 8(c)). This is potentially attributable to the adiabatic thermal boundary condition: indeed, wall temperature gradients can induce high compressibility effects, which are weaker in case of adiabatic walls. Numerical investigation of isothermal, cooled wall flows is a challenging task due to the uncertainty about turbulence term closure. This goes beyond the scope of the preliminary analysis of this work and is still an ongoing task.

Similarly to the low-enthalpy case, the two contributions of the turbulent kinetic energy production term are reported in Fig. 9 for the source 2, confirming the change of sign is given by P_{k2}. Also, the turbulent viscosity ratio is shown in Fig. 10.

Wall quantity profiles (pressure and shear stress) are shown in Fig. 11. Again, the source 2 leads to an overestimation of the separation bubble, while underestimating the wall shear stress.

Given this opposite behavior of the two expressions of P'_k, it is fundamental to understand which are the consequences on the chemical dissociation activity. Contours of N_2 and O_2 mass fractions and vibrational temperatures are shown in Fig. 12. The pictures are zoomed near the compression corner to better observe the differences between the two approaches. First of all, the stronger compressibility effects promoted by the source 2 are evident also on the chemical activity, as the dissociation is more pronounced in such a case. Both molecular nitrogen and oxygen dissociation are

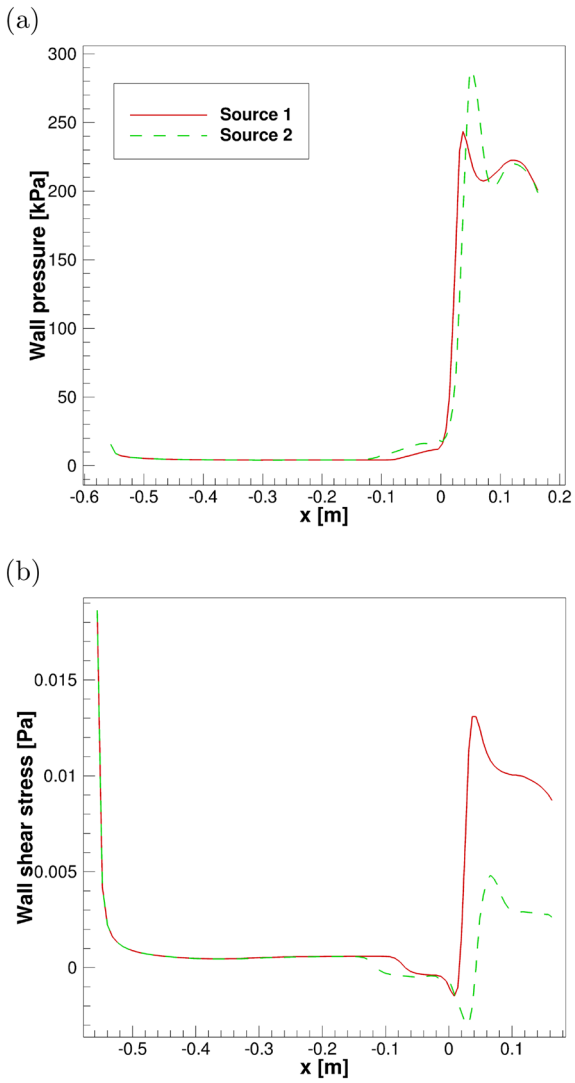

Fig. 11 Comparison of pressure (**a**) and shear stress (**b**) profiles for different expression of the turbulent kinetic energy production term

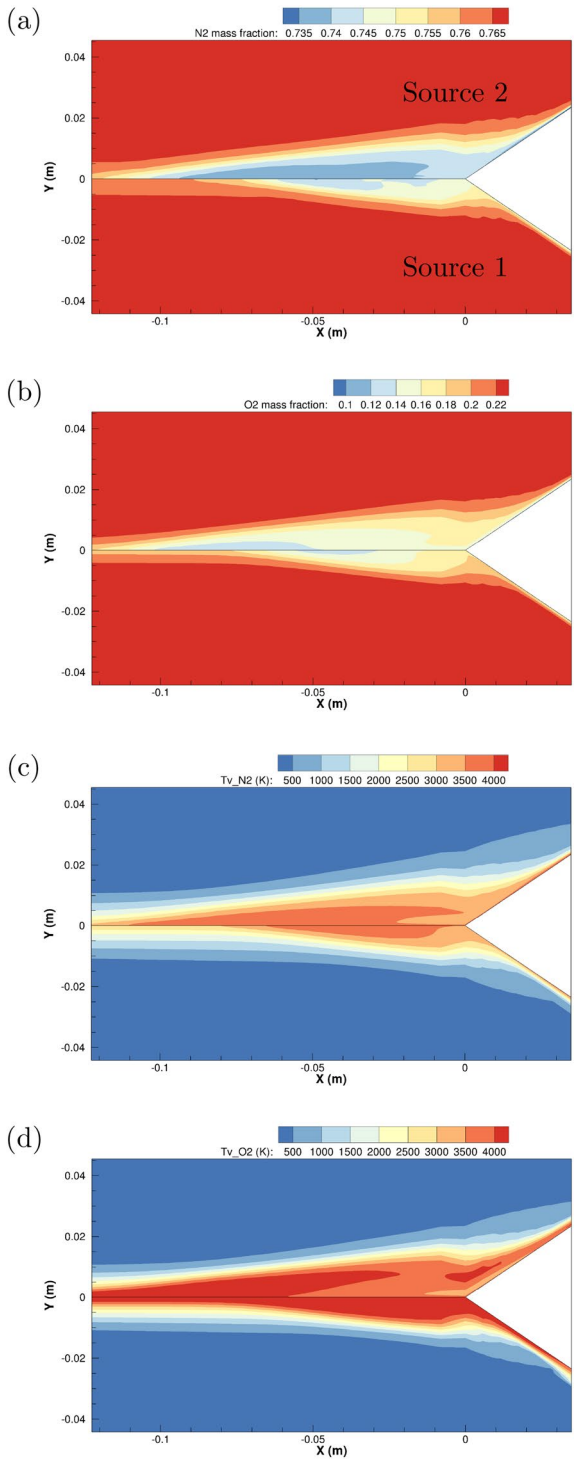

Fig. 12 Comparison of N_2 mass fraction (**a**), O_2 mass fraction (**b**), T_{v,N_2} (**c**) and T_{v,O_2} (**d**) for different expressions of the turbulent kinetic energy production term

more relevant in the case of source 2; moreover, they are anticipated given the bigger size of the separation bubble.

However, no relevant differences are observed in the contours of the vibrational temperatures: besides the different separation bubble extent, the values are mostly comparable in both cases.

4 Conclusions

In this paper, preliminary numerical results for hypersonic turbulent boundary layer have been presented. Turbulent shock wave/boundary layer interaction has been simulated, underlining the influence of high-enthalpy effects. Turbulence has been modeled by means of the standard SST $k-\omega$ model, which well describes the physics of the boundary layer in the presence of relevant curvature of the geometry.

The results showed good agreement with experimental findings and numerical references in the literature. However, they are strongly affected by the expression of the turbulent kinetic energy production term. Depending on how this term is modeled, compressibiltiy effects and chemical activity change, leading to a different separation bubble extent in the case of a compression ramp flow. However, this assessment needs further investigations.

Finally, in the context of hypersonic turbulent boundary layer studies, a tuning of the classical turbulence models has to be devised, in order to improve the quality of the solution obtained by numerical simulations with no need of performing a DNS, whose practical applications are limited due to their huge computational cost. Needless to say DNS studies are essential to provide a sufficiently wide range of data to make turbulence models training feasible in the most common configurations, such as flat plate and shock wave/boundary layer interaction.

Acknowledgements D. Ninni, F. Bonelli and G. Pascazio were partially supported by the Italian Ministry of Education, University and Research under the Program Department of Excellence Legge 232/2016 (Grant No. CUP–D93C23000100001). The authors also acknowledge the CINECA award under the ISCRA initiative, for the availability of high-performance computing resources and support under the allocation HP10CROAPG.

Funding Open access funding provided by Politecnico di Bari within the CRUI-CARE Agreement.

Data availability No data is available.

Declarations

Conflicts of Interest All authors have no conflicts of interest.

Open Access This article is licensed under a Creative Commons Attribution 4.0 International License, which permits use, sharing, adaptation, distribution and reproduction in any medium or format, as long as you give appropriate credit to the original author(s) and the source, provide a link to the Creative Commons licence, and indicate if changes were made. The images or other third party material in this article are included in the article's Creative Commons licence, unless indicated otherwise in a credit line to the material. If material is not included in the article's Creative Commons licence and your intended use is not permitted by statutory regulation or exceeds the permitted use, you will need to obtain permission directly from the copyright holder. To view a copy of this licence, visit http://creativecommons.org/licenses/by/4.0/.

References

1. Leyva, I.A.: The relentless pursuit of hypersonic flight. Phys. Today **70**(11), 30–36 (2017)
2. Candler, G.V.: Rate effects in hypersonic flows. Annu. Rev. Fluid Mech. **51**, 379–402 (2019)
3. Bertin, J.J., Cummings, R.M.: Critical hypersonic aerothermodynamic phenomena. Annu. Rev. Fluid Mech. **38**, 129 (2006)
4. Guo, Y., Adams, N.A.: Numerical investigation of supersonic turbulent boundary layers with high wall temperature. Stanford Univ., Studying Turbulence Using Numerical Simulation Databases. 5: Proceedings of the 1994 Summer Program (1994)
5. Guarini, S.E., Moser, R.D., Shariff, K., Wray, A.: Direct numerical simulation of a supersonic turbulent boundary layer at Mach 2.5. Journal of Fluid Mechanics 414, 1–33 (2000)
6. Maeder, T., Adams, N.A., Kleiser, L.: Direct simulation of turbulent supersonic boundary layers by an extended temporal approach. J. Fluid Mech. **429**, 187–216 (2001)
7. Pirozzoli, S., Grasso, F., Gatski, T.: Direct numerical simulation and analysis of a spatially evolving supersonic turbulent boundary layer at M=2.25. Physics of fluids **16**(3), 530–545 (2004)
8. Martin, M.P.: Direct numerical simulation of hypersonic turbulent boundary layers. Part 1. Initialization and comparison with experiments. Journal of Fluid Mechanics 570, 347–364 (2007)
9. Duan, L., Beekman, I., Martin, M.: Direct numerical simulation of hypersonic turbulent boundary layers. Part 2. Effect of wall temperature. Journal of Fluid Mechanics 655, 419–445 (2010)
10. Duan, L., Beekman, I., Martin, M.: Direct numerical simulation of hypersonic turbulent boundary layers. Part 3. Effect of Mach number. Journal of Fluid Mechanics 672, 245–267 (2011)
11. Franko, K.J., Lele, S.K.: Breakdown mechanisms and heat transfer overshoot in hypersonic zero pressure gradient boundary layers. J. Fluid Mech. **730**, 491–532 (2013)
12. Sciacovelli, L., Passiatore, D., Cinnella, P., Pascazio, G.: Assessment of a high-order shock-capturing central-difference scheme for hypersonic turbulent flow simulations. Computers & Fluids **230**, 105134 (2021)
13. Stemmer, C., Mansour, N.: DNS of transition in hypersonic boundary-layer flows including high-temperature gas effects. Annual Research Briefs **2001**, 143–150 (2001)
14. Duan, L., Martin, M.: Direct numerical simulation of hypersonic turbulent boundary layers. Part 4. Effect of high enthalpy. Journal of Fluid Mechanics 684, 25–59 (2011)
15. Passiatore, D., Sciacovelli, L., Cinnella, P., Pascazio, G.: Finite-rate chemistry effects in turbulent hypersonic boundary layers: A direct numerical simulation study. Physical Review Fluids **6**(5), 054604 (2021)
16. Morkovin, M.V.: Effects of compressibility on turbulent flows. Mécanique de la Turbulence **367**(380), 26 (1962)
17. Van Driest, E.R.: Turbulent boundary layer in compressible fluids. J Aeronautical Sci **18**(3), 145–160 (1951)
18. Van Driest, E.R.: On turbulent flow near a wall. J Aeronautical sci **23**(11), 1007–1011 (1956)
19. Van Driest, E.R.: The Problem of Aerodynamic Heating, (1956)
20. Di Renzo, M., Urzay, J.: Direct numerical simulation of a hypersonic transitional boundary layer at suborbital enthalpies. J. Fluid Mech. **912**, 29 (2021)
21. Passiatore, D., Sciacovelli, L., Cinnella, P., Pascazio, G.: Thermochemical non-equilibrium effects in turbulent hypersonic boundary layers. Journal of Fluid Mechanics **941** (2022)
22. Sciacovelli, L., Cinnella, P., Gloerfelt, X.: Direct numerical simulations of supersonic turbulent channel flows of dense gases. J. Fluid Mech. **821**, 153–199 (2017)
23. Coleman, G., Stollery, J.: Heat transfer from hypersonic turbulent flow at a wedge compression corner. J. Fluid Mech. **56**(4), 741–752 (1972)
24. Knight, D., Mortazavi, M.: Hypersonic shock wave transitional boundary layer interactions-A review. Acta Astronaut. **151**, 296–317 (2018)
25. Currao, G.M., Choudhury, R., Gai, S.L., Neely, A.J., Buttsworth, D.R.: Hypersonic transitional shock-wave-boundary-layer interaction on a flat plate. AIAA J. **58**(2), 814–829 (2020)

26. Schülein, E.: Skin friction and heat flux measurements in shock/boundary layer interaction flows. AIAA J. **44**(8), 1732–1741 (2006)
27. Sandham, N., Schülein, E., Wagner, A., Willems, S., Steelant, J.: Transitional shock-wave/boundary-layer interactions in hypersonic flow. J. Fluid Mech. **752**, 349–382 (2014)
28. Passiatore, D., Sciacovelli, L., Cinnella, P., Pascazio, G.: Shock impingement on a transitional hypersonic high-enthalpy boundary layer. Phys Rev Fluids **8**(4), 044601 (2023)
29. Grasso, F., Falconi, D.: High-speed turbulence modeling of shock-wave/boundary-layer interaction. AIAA J. **31**(7), 1199–1206 (1993)
30. John, B., Kulkarni, V.N., Natarajan, G.: Shock wave boundary layer interactions in hypersonic flows. Int. J. Heat Mass Transf. **70**, 81–90 (2014)
31. Priebe, S., Martín, M.P.: Turbulence in a hypersonic compression ramp flow. Phys Rev Fluids **6**(3), 034601 (2021)
32. Tong, F., Duan, J., Li, X.: Shock wave and turbulent boundary layer interaction in a double compression ramp. Computers & Fluids **229**, 105087 (2021)
33. Lugrin, M., Beneddine, S., Leclercq, C., Garnier, E., Bur, R.: Transition scenario in hypersonic axisymmetrical compression ramp flow. J. Fluid Mech. **907**, 6 (2021)
34. Cao, S., Hao, J., Klioutchnikov, I., Wen, C.-Y., Olivier, H., Heufer, K.A.: Transition to turbulence in hypersonic flow over a compression ramp due to intrinsic instability. J. Fluid Mech. **941**, 8 (2022)
35. Grasso, F., Marini, M., Ranuzzi, G., Cuttica, S., Chanetz, B.: Shock-wave/turbulent boundary-layer interactions in nonequilibrium flows. AIAA J. **39**(11), 2131–2140 (2001)
36. Volpiani, P.S.: Numerical strategy to perform direct numerical simulations of hypersonic shock/boundary-layer interaction in chemical nonequilibrium. Shock Waves **31**(4), 361–378 (2021)
37. Jiang, H., Liu, J., Luo, S., Huang, W., Wang, J., Liu, M.: Thermochemical non-equilibrium effects on hypersonic shock wave/turbulent boundary-layer interaction. Acta Astronaut. **192**, 1–14 (2022)
38. Tumuklu, O., Levin, D.A., Theofilis, V.: Modal analysis with proper orthogonal decomposition of hypersonic separated flows over a double wedge. Phys Rev Fluids **4**(3), 033403 (2019)
39. Cao, S., Hao, J., Klioutchnikov, I., Olivier, H., Wen, C.-Y.: Unsteady effects in a hypersonic compression ramp flow with laminar separation. J. Fluid Mech. **912**, 3 (2021)
40. Wilcox, D.C., : Turbulence Modeling for CFD vol. 2, (1998)
41. Park, C.: Nonequilibrium Hypersonic Aerothermodynamics (1990)
42. Pascazio, G., Ninni, D., Bonelli, F., Colonna, G.: Hypersonic flows with detailed state-to-state kinetics using a GPU cluster. In: Plasma Modeling (Second Edition): Methods and Applications, (2022)
43. Zhang, X.-H., Wu, Y.-Z., Wang, J.-F.: Turbulence models for accurate aerothermal prediction in hypersonic flows. Mod. Phys. Lett. B **24**(13), 1345–1348 (2010)
44. Tu, G., Deng, X., Mao, M.: Assessment of two turbulence models and some compressibility corrections for hypersonic compression corners by high-order difference schemes. Chin. J. Aeronaut. **25**(1), 25–32 (2012)
45. Menter, F.R., Kuntz, M., Langtry, R.: Ten years of industrial experience with the SST turbulence model. Turbulence, Heat Mass Trans **4**(1), 625–632 (2003)
46. Ninni, D., Bonelli, F., Colonna, G., Pascazio, G.: Unsteady behavior and thermochemical non equilibrium effects in hypersonic double-wedge flows. Acta Astronaut. **191**, 178–192 (2022)
47. Wilke, C.: A viscosity equation for gas mixtures. J. Chem. Phys. **18**(4), 517–519 (1950)
48. Gupta, R.N., Lee, K.-P., Thompson, R.A., Yos, J.M.: A review of reaction rates and thermodynamic and transport properties for an 11-species air model for chemical and thermal nonequilibrium calculations to 30000 K (1990)
49. https://turbmodels.larc.nasa.gov/sst.html
50. Mason, E., Saxena, S.: Approximate formula for the thermal conductivity of gas mixtures. Phys fluids **1**(5), 361–369 (1958)
51. Srivastava, B., Srivastava, R.: Thermal conductivity and Eucken correction for diatomic gases and binary gas mixtures. J. Chem. Phys. **30**(5), 1200–1205 (1959)
52. Menter, F.R.: Two-equation eddy-viscosity turbulence models for engineering applications. AIAA J. **32**(8), 1598–1605 (1994)
53. Steger, J.L., Warming, R.: Flux vector splitting of the inviscid gas-dynamic equations with application to finite-difference methods. J. Comput. Phys. **40**(2), 263–293 (1981)
54. Van Leer, B.: Towards the ultimate conservative difference scheme. V.A second-order sequel to Godunov's method. J Comput Phys **32**(1), 101–136 (1979)
55. Harten, A.: High resolution schemes for hyperbolic conservation laws. J. Comput. Phys. **135**(2), 260–278 (1997)
56. Jiang, G.-S., Shu, C.-W.: Efficient implementation of weighted ENO schemes. J. Comput. Phys. **126**(1), 202–228 (1996)
57. Verwer, J.G.: Gauss-Seidel iteration for stiff ODEs from chemical kinetics. SIAM J. Sci. Comput. **15**(5), 1243–1250 (1994)
58. Marvin, J.G., Brown, J.L., Gnoffo, P.A.: Experimental database with baseline CFD solutions: 2-D and axisymmetric hypersonic shock-wave/turbulent-boundary-layer interactions. Technical report (2013)
59. Liu, M., Han, G., Jiang, Z.: Experimental investigation on plate boundary layer transition in jf-12 hypersonic shock tunnel. 32rd ISSW (2019)
60. Roy, C.J., Blottner, F.G.: Review and assessment of turbulence models for hypersonic flows. Prog. Aerosp. Sci. **42**(7–8), 469–530 (2006)
61. Tian, Y., Gao, Z., Jiang, C., Lee, C.-H.: A correction for Reynolds-averaged-Navier-Stokes turbulence model under the effect of shock waves in hypersonic flows. Int. J. Numer. Meth. Fluids **95**(2), 313–333 (2023)

Publisher's Note Springer Nature remains neutral with regard to jurisdictional claims in published maps and institutional affiliations.